Chemical Science

EDGE ARTICLE

View Article Online
View Journal | View Issue

Cite this: *Chem. Sci.*, 2017, **8**, 795

Epitaxial growth of unusual 4H hexagonal Ir, Rh, Os, Ru and Cu nanostructures on 4H Au nanoribbons†

Zhanxi Fan,‡[a] Ye Chen,‡[a] Yihan Zhu,‡[b] Jie Wang,[a] Bing Li,[c] Yun Zong,[c] Yu Han[b] and Hua Zhang*[a]

Received 5th July 2016
Accepted 10th September 2016

DOI: 10.1039/c6sc02953a

www.rsc.org/chemicalscience

Metal nanomaterials normally adopt the same crystal structure as their bulk counterparts. Herein, for the first time, the unusual 4H hexagonal Ir, Rh, Os, Ru and Cu nanostructures have been synthesized on 4H Au nanoribbons (NRBs) *via* solution-phase epitaxial growth under ambient conditions. Interestingly, the 4H Au NRBs undergo partial phase transformation from 4H to face-centered cubic (fcc) structures after the metal coating. As a result, a series of polytypic 4H/fcc bimetallic Au@M (M = Ir, Rh, Os, Ru and Cu) core–shell NRBs has been obtained. We believe that the rational crystal structure-controlled synthesis of metal nanomaterials will bring new opportunities for exploring their phase-dependent physicochemical properties and promising applications.

Introduction

Metal nanomaterials have attracted wide attention because of their exceptional optical, magnetic and electronic properties associated with many promising applications like energy conversion, surface-enhanced Raman scattering, biosensing, photo-thermal therapy, ultrahigh-density data storage and catalysis.[1–6] As is known, the physicochemical properties of metal nanomaterials are regulated by their size, shape and composition.[2] Importantly, recent experimental investigations suggest that crystal phases of metal nanomaterials can have remarkable impact on their various functional properties.[7,8] For instance, along with a change of crystal structures from the common face-centered cubic (fcc) phase to the unusual face-centered tetragonal (fct) phase, the magnetic properties of FePt nanoparticles completely change from superparamagnetic properties to strongly ferromagnetic properties.[9] Another study found that fcc Ru nanoparticles with a size larger than 3.0 nm exhibit higher catalytic activity in CO oxidation in comparison with the common hexagonal close-packed (hcp, 2H type) Ru nanoparticles with a similar size.[10] Therefore, besides the well established size, shape and composition control, the phase control of different metal nanomaterials could provide a new effective strategy to boost their various properties and broaden their applications. However, it is still a great challenge to attain crystal structure-controlled synthesis of metal nanomaterials, in particular under ambient conditions.

Epitaxial growth refers to the oriented deposition of a crystalline material over a crystalline substrate, which can be used to synthesize new crystal structures of the deposited material.[11,12] Conventionally, vapor-phase epitaxial growth has been widely used to prepare metastable crystal structures of metal thin films on different substrates, such as body-centered cubic (bcc) Cu on Fe,[13] fcc Co on Cu,[14] and bcc Pd on W.[15] Unfortunately, the vapor-phase epitaxial growth method used for preparation of the metastable crystal structures of metals always involves harsh experimental conditions like ultra-high vacuum and high temperature,[13–15] which can induce the aggregation/degradation of ultrathin anisotropic metal nanomaterials and thus make it not suitable for their crystal structure-controlled synthesis. Recently, solution-phase epitaxial growth, which holds the advantage of mild experimental conditions, has been developed for the size-, shape- and composition-controlled synthesis of bimetallic core–shell nanomaterials, such as Pt@Pd,[16] Au@Pd,[17,18] Pd@Pt,[19] Au@Ag,[17,20] Pd@Ir,[21] Au@Rh,[22] and Au@Ni.[23] However, all the aforementioned epitaxially grown metal shells crystallize in the same crystal phases as their bulk counterparts, *i.e.* fcc phase. To date, the development of the solution-phase epitaxial growth of new crystal structures of metal nanomaterials remains primitive.

Recently, we first demonstrated the facile wet chemical synthesis of ultrathin hcp Au square sheets,[24] and then 4H hexagonal Au nanoribbons (NRBs).[25] By using the aforementioned Au nanostructures as seeds, the hcp Ag,[26] and 4H

[a]*Center for Programmable Materials, School of Materials Science and Engineering, Nanyang Technological University, 50 Nanyang Avenue, Singapore 639798, Singapore. E-mail: hzhang@ntu.edu.sg; Web: http://www.ntu.edu.sg/home/hzhang/*

[b]*Advanced Membranes and Porous Materials Center, Physical Sciences and Engineering Division, King Abdullah University of Science and Technology, Thuwal 23955-6900, Saudi Arabia*

[c]*Institute of Materials Research and Engineering, Agency for Science, Technology and Research (A*STAR), 2 Fusionopolis Way, Innovis #08-03, Singapore 138634, Singapore*

† Electronic supplementary information (ESI) available: Experimental section including materials, synthesis and characterization, and supporting data. See DOI: 10.1039/c6sc02953a

‡ These authors contributed equally to this work.

hexagonal Ag, Pd and Pt have been prepared *via* the metal coating strategy,[25] and the 4H hexagonal PtAg, PdAg and PtPdAg alloy nanostructures have also been synthesized *via* a galvanic reaction method.[27] It should be mentioned that the lattice mismatch between Au and Ag, Pd or Pt is relatively small (usually less than 5%).[17,18,20] However, owing to the relatively large lattice mismatch between Au and the other metals, such as Ir, Rh, Os, Ru and Cu, their epitaxial growth on non-fcc Au nanostructures has not been achieved. Here, for the first time, we report the solution-phase epitaxial growth of novel 4H hexagonal Ir, Rh, Os, Ru and Cu on 4H Au NRBs under ambient conditions. Meanwhile, a partial phase change from 4H to fcc structures is observed in Au NRBs after the metal coating. As a result, the corresponding five kinds of bimetallic core–shell NRBs with an unusual 4H/fcc crystal structure are obtained.

Results and discussion

In our experiment, the 4H hexagonal Au NRBs were first synthesized by using our recently developed approach with a little modification (see Experimental section in the ESI for details†).[25] The typical transmission electron microscope (TEM) images and corresponding selected-area electron diffraction (SAED) pattern show that Au NRBs with an unusual 4H crystal phase were successfully prepared (Fig. S1a–c†). Simultaneously, the 4H crystal structure of Au NRBs was further confirmed by the representative high-resolution TEM (HRTEM) image (Fig. S1d†), which is in agreement with our former report.[25] Then the obtained 4H hexagonal Au NRBs served as templates for the solution-phase epitaxial growth of 4H hexagonal structures of Ir, Rh, Os, Ru and Cu. As a result, the polytypic 4H/fcc bimetallic Au@M (M = Ir, Rh, Os, Ru and Cu) core–shell NRBs were formed due to the partial 4H-to-fcc phase transition of Au NRBs during the metal coating (Fig. 1).

Taking Ir as a representative example, the solution-phase epitaxial growth of 4H hexagonal Ir was achieved by reducing $IrCl_3$ with $NaBH_4$ in the presence of 4H Au NRBs and iodide ions under ambient conditions (see Experimental section in the ESI for details†). After the reduction reaction, the surface of Au NRBs becomes relatively rough, indicating the successful coating of Ir on Au NRBs (Fig. 2a and b). X-ray photoelectron spectroscopy (XPS) revealed the chemical states of Au(0) and Ir(0) in the Au@Ir NRBs (Fig. S2†). The elemental composition of Au@Ir NRBs was studied by scanning TEM-energy dispersive X-ray spectroscopy (STEM-EDS), which exhibits an average Au/Ir molar ratio of approximately 1.00/0.99 (Fig. S3†). A typical high-angle annular dark-field-STEM (HAADF-STEM) image (Fig. 2e) and corresponding STEM-EDS element maps (Fig. 2f–h) demonstrate that the Ir shell was continuously formed on the Au core, which is also verified by the STEM-EDS line scan profile (Fig. S4†). These observations suggest that the coating of Ir on the surface of 4H Au NRBs might follow the intermediate type of growth, *i.e.* the so-called Stranski–Krastanov (S–K) mode.[28] The average thickness of the Ir shell is estimated to be around 3.9 nm (Fig. 2b). Impressively, a representative SAED pattern of the obtained Au@Ir NRB shows a characteristic diffraction pattern of $[110]_{4H}$ zone, coexisting with some diffraction streaks in the $[001]_{4H}$ close-packed direction (Fig. 2c). The presence of diffraction streaks in the SAED pattern suggests the formation of fcc domains and stacking faults/twins in the $[001]_{4H}/[111]_f$ directions (Fig. 2c). Such a kind of phase transition, *i.e.* from $(110)_{4H}$-oriented 4H hexagonal to $(101)_f$-oriented fcc phases, can be achieved *via* the movement of partial dislocations on close-packed planes.[29] During the phase transition of Au NRBs from

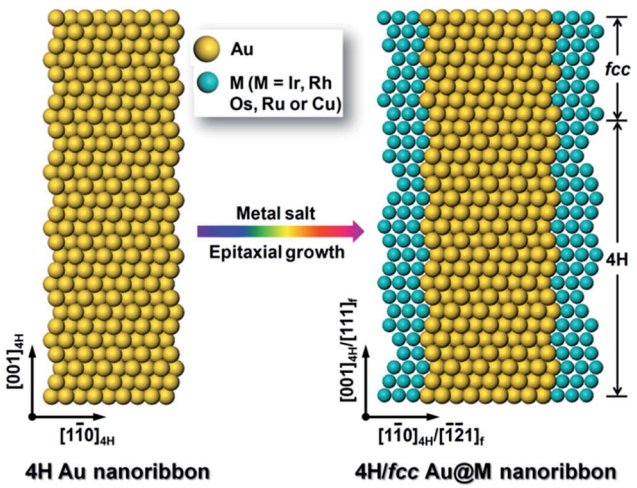

Fig. 1 A schematic illustration of the solution-phase epitaxial growth of 4H hexagonal Ir, Rh, Os, Ru and Cu nanostructures on 4H Au NRBs.

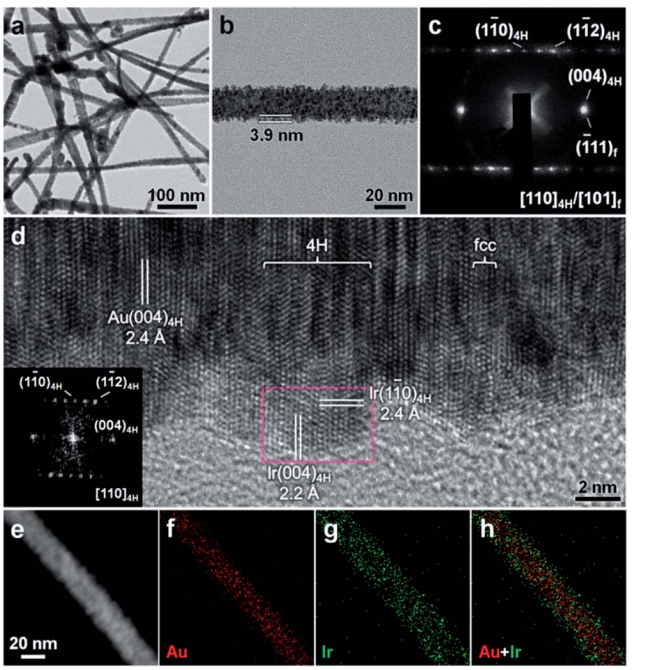

Fig. 2 (a) Low-magnification TEM image of alternating 4H/fcc bimetallic Au@Ir core–shell NRBs. (b) High-magnification TEM image and (c) the corresponding SAED pattern of a representative Au@Ir NRB. (d) A representative HRTEM image of Au@Ir NRBs. Inset: the corresponding FFT pattern of the selected region, *i.e.* the magenta dashed rectangle in (d). (e) HAADF-STEM image, and (f–h) corresponding STEM-EDS element maps of a representative Au@Ir NRB.

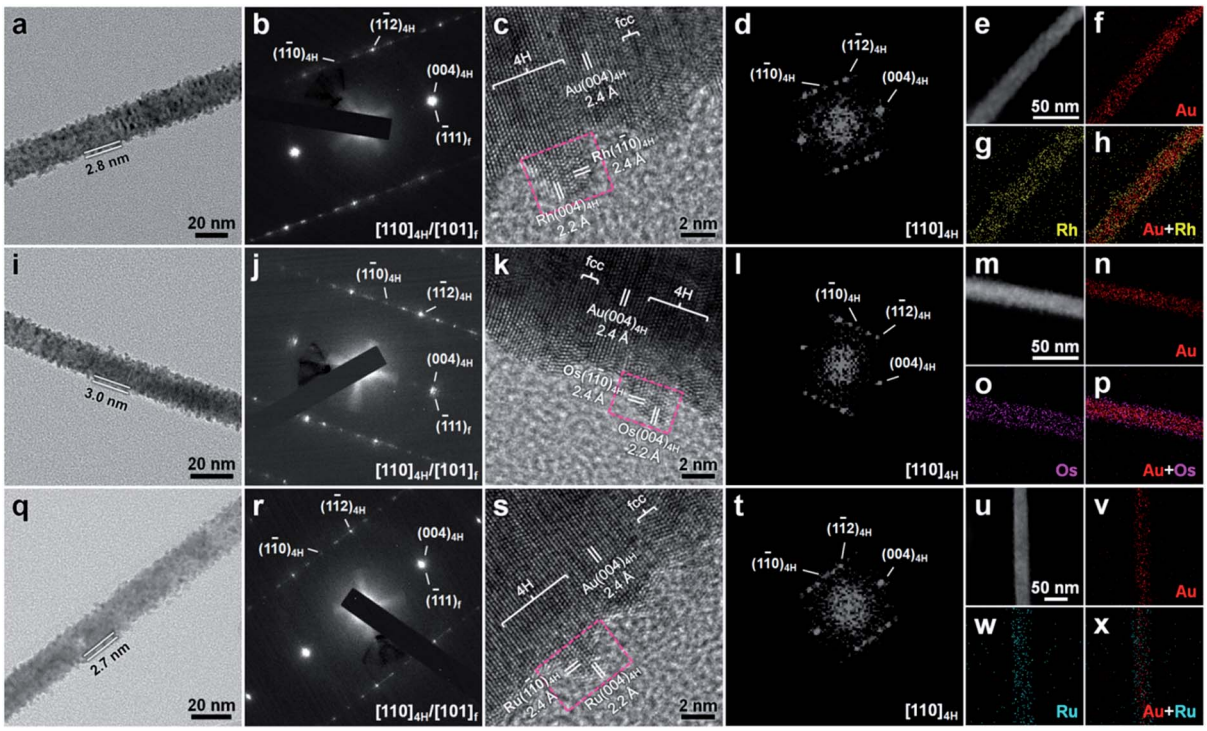

Fig. 3 (a) TEM image, (b) SAED pattern, and (c) HRTEM image of a representative 4H/fcc bimetallic Au@Rh core–shell NRB. (d) The corresponding FFT pattern of the selected region, *i.e.* the magenta dashed rectangle in (c). (e) HAADF-STEM image, and (f–h) corresponding STEM-EDS element maps of a representative Au@Rh NRB. (i) TEM image, (j) SAED pattern, and (k) HRTEM image of a representative 4H/fcc bimetallic Au@Os core–shell NRB. (l) The corresponding FFT pattern of the selected region, *i.e.* the magenta dashed rectangle in (k). (m) HAADF-STEM image, and (n–p) corresponding STEM-EDS element maps of a representative Au@Os NRB. (q) TEM image, (r) SAED pattern, and (s) HRTEM image of a representative 4H/fcc bimetallic Au@Ru core–shell NRB. (t) The corresponding FFT pattern of the selected region, *i.e.* the magenta dashed rectangle in (s). (u) HAADF-STEM image, and (v–x) corresponding STEM-EDS element maps of a representative Au@Ru NRB.

4H to fcc structures, the close-packed directions, *i.e.* $[001]_{4H}$ and $[111]_f$ directions, are preserved. The partial structure change of Au NRBs from the 4H hexagonal to fcc phases might be caused by the epitaxial strain between Au and Ir.[12,25,26,30–32] Importantly, the Ir shell is epitaxially grown on the Au core since no other randomly distributed diffraction spot is found (Fig. 2c). To further investigate the crystal structure of Au@Ir NRBs, a HRTEM image was also collected, which clearly shows the alternating intergrowth of 4H and fcc structures (Fig. 2d). The coexistence of 4H and fcc phases in Au@Ir NRBs is also confirmed by the X-ray diffraction (XRD) pattern (Fig. S5†). An inter-planar distance of 2.4 Å is assigned to the lattice spacing of close-packed planes in $[001]_{4H}/[111]_f$ directions (Fig. 2d). Meanwhile, it can be clearly seen that the lattice fringe coherently extends from the inside Au core to the outside Ir shell, indicating the epitaxial relation between them (Fig. 2d). Furthermore, the corresponding selected-area fast Fourier transform (FFT) of the HRTEM image shows a typical $[110]_{4H}$-zone diffraction pattern, indicating the successful synthesis of the 4H hexagonal structure of Ir (inset in Fig. 2d). The lattice spacings of 2.2 Å and 2.4 Å can be attributed to the $(004)_{4H}$ and $(1\bar{1}0)_{4H}$ planes of 4H Ir, respectively (Fig. 2d). It should be noted that bulk Ir crystals adopt the normal high-symmetry fcc phase.[33] This is the first time that an Ir nanostructure with an unusual 4H hexagonal crystal phase has been synthesized, which possesses a representative stacking order of "ABCB" in the $[001]_{4H}$ close-packed direction.

Impressively, by replacing the metal salt of $IrCl_3$ with $RhCl_3$, $OsCl_3$ or $RuCl_3$, similar to the aforementioned Ir nanostructure, the unusual 4H hexagonal structure of Rh, Os or Ru can also be synthesized by the epitaxial growth on as-prepared 4H Au NRBs under ambient conditions (see the Experimental section in the ESI for details†). Note that the bulk crystals of Rh, Os and Ru crystallize in the fcc, hcp and hcp phases, respectively.[33] Fig. 3a shows the TEM image of a representative Au@Rh NRB. The Rh shell, with an average thickness of around 2.8 nm (Fig. 3a), epitaxially grows on the Au core (Fig. 3b and c). The SAED pattern and HRTEM image of bimetallic Au@Rh NRBs suggest an alternating intergrowth of 4H hexagonal and fcc structures along the close-packed directions of $[001]_{4H}/[111]_f$ (Fig. 3b and c). The selected-area FFT pattern of the HRTEM image confirms the successful formation of 4H hexagonal Rh (Fig. 3d). The lattice distances of 2.2 Å and 2.4 Å can be attributed to the $(004)_{4H}$ and $(1\bar{1}0)_{4H}$ planes of 4H Rh, respectively (Fig. 3c). The average Au/Rh molar ratio is approximately 1.00/0.75 (Fig. S6†). The HAADF-STEM image and corresponding STEM-EDS element maps and line scan curves further identify the successful formation of the Rh shell on the Au core (Fig. 3e–h and S7†). Fig. 3i shows a typical TEM image of an Au@Os NRB. The average thickness of the Os shell is around 3.0 nm (Fig. 3i). The epitaxial relation between Au and Os, and the coexistence of 4H and fcc structures in Au@Os NRBs are proved by the SAED pattern and HRTEM image (Fig. 3j and k). The successful formation of 4H

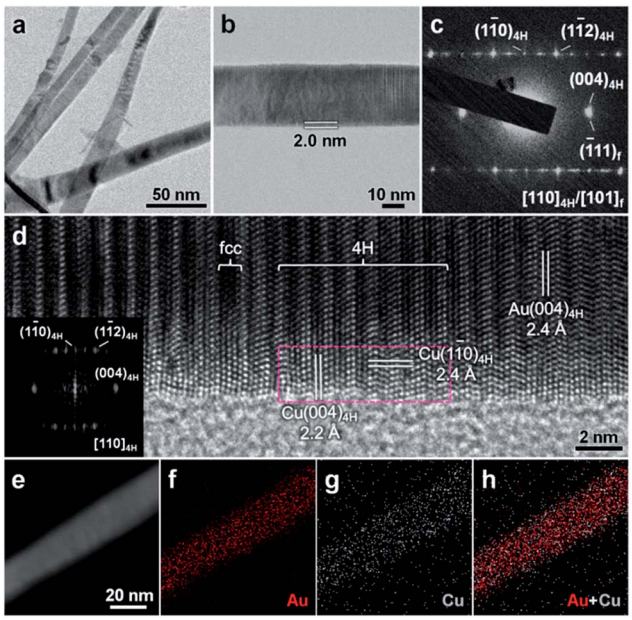

Fig. 4 (a) Low-magnification TEM image of alternating 4H/fcc bimetallic Au@Cu core–shell NRBs. (b) High-magnification TEM image and (c) corresponding SAED pattern of a representative Au@Cu NRB. (d) A representative HRTEM image of Au@Cu NRBs. Inset: the corresponding FFT pattern of the selected region, *i.e.* the magenta dashed rectangle in (d). (e) HAADF-STEM image, and (f–h) corresponding STEM-EDS element maps of a representative Au@Cu NRB.

hexagonal Os is confirmed by the selected-area FFT pattern of the HRTEM image (Fig. 3l). The inter-plane spacings of 2.2 Å and 2.4 Å can be assigned to the $(004)_{4H}$ and $(1\bar{1}0)_{4H}$ planes of 4H Os, respectively (Fig. 3k). The average Au/Os molar ratio is approximately 1.00/0.81 (Fig. S8†). The homogeneous growth of Os on Au NRBs is further corroborated by the HAADF-STEM image and STEM-EDS analysis (Fig. 3m–p and S9†). Fig. 3q shows a representative TEM image of an Au@Ru NRB. The average thickness of the Ru shell is around 2.7 nm (Fig. 3q). Similarly, the Ru shell is also epitaxially grown on the Au core, and Au@Ru NRBs also exhibit the alternating 4H/fcc structures (Fig. 3r and s). Meanwhile, the 4H hexagonal structure of Ru has also been observed (Fig. 3t). The lattice distances of 2.2 Å and 2.4 Å can be attributed to the $(004)_{4H}$ and $(1\bar{1}0)_{4H}$ planes of 4H Ru, respectively (Fig. 3s). The average Au/Ru molar ratio is approximately 1.00/0.71 (Fig. S10†). The HAADF-STEM image and corresponding STEM-EDS analysis further confirm the uniform deposition of Ru on Au NRBs (Fig. 3u–x and S11†). Additionally, the chemical states of Au(0) and Rh(0), Au(0) and Os(0), and Au(0) and Ru(0) in the aforementioned Au@Rh, Au@Os, and Au@Ru NRBs, respectively, were revealed by XPS (Fig. S12†). The coexistence of 4H and fcc phases in Au@Rh, Au@Os and Au@Ru NRBs is proven by the XRD pattern (Fig. S13†).

Remarkably, besides the aforementioned four noble metals, *i.e.* Ir, Rh, Os and Ru, our solution-phase epitaxial growth strategy can also be used to synthesize the 4H hexagonal structure of common transition metals. As a representative example, Cu was chosen in our experiment. Briefly, the epitaxial growth of 4H hexagonal Cu was achieved by reducing $Cu(NO_3)_2$ with $NaBH_4$ in the presence of 4H Au NRBs under ambient conditions (see Experimental section in the ESI for details†). XPS revealed the chemical states of Au(0) and Cu(0) in the obtained Au@Cu NRBs (Fig. S14†). Fig. 4a shows a representative TEM image of Au NRBs after coating with Cu. The obtained Cu shell shows a relatively smooth surface and has an average thickness of around 2.0 nm (Fig. 4b). The elemental composition of as-prepared Au@Cu NRBs was investigated by STEM-EDS, exhibiting an average Au/Cu molar ratio of approximately 1.00/0.45 (Fig. S15†). The typical HAADF-STEM image (Fig. 4e) and corresponding STEM-EDS element maps (Fig. 4f–h) of an Au@Cu NRB show the continuous coating of Cu on Au NRBs, which is also identified by STEM-EDS line scan curves (Fig. S16†). These results indicate that the coating of Cu on the surface of 4H Au NRBs might proceed *via* layered growth, *i.e.* the so-called Frank–van der Merwe (F–M) mode.[28] Notably, the SAED pattern of a representative Au@Cu NRB reveals the coexistence of 4H/fcc structures and the epitaxial relation between Au and Cu (Fig. 4c), which has been further confirmed by a representative HRTEM image (Fig. 4d). The coexistence of 4H and fcc phases in Au@Cu NRBs is also identified by the XRD pattern (Fig. S17†). A lattice distance of 2.4 Å is assigned to close-packed planes in the $[001]_{4H}/[111]_f$ directions (Fig. 4d). Significantly, the selected-area FFT pattern demonstrates a characteristic diffraction pattern in the $[110]_{4H}$ zone, suggesting that the 4H hexagonal structure of Cu is successfully formed (inset in Fig. 4d). The lattice spacings of 2.2 Å and 2.4 Å can be attributed to the $(004)_{4H}$ and $(1\bar{1}0)_{4H}$ planes of 4H Cu, respectively (Fig. 4d). Note that bulk Cu crystals demonstrate the common high-symmetry fcc phase.[33] This is the first time a Cu nanostructure with a unique 4H hexagonal phase has been synthesized.

Conclusions

In summary, by using 4H Au NRBs as templates, we have successfully synthesized unusual 4H hexagonal structures of Ir, Rh, Os, Ru and Cu with a facile solution-phase epitaxial growth strategy under ambient conditions. Meanwhile, a partial 4H-to-fcc phase transition in the 4H Au NRBs is observed after metal deposition on their surface. As a result, a new class of alternating 4H/fcc bimetallic core–shell NRBs, *i.e.* Au@Ir, Au@Rh, Au@Os, Au@Ru and Au@Cu NRBs, has been obtained. It is expected that the as-prepared metal nanomaterials with novel crystal structures might have some promising applications in electrocatalysis[5,6,19,34] and energy conversion.[1] Importantly, our findings suggest that the solution-based templated growth of novel nanostructures with new crystal phases provides a universal strategy for the crystal-phase controlled synthesis of various metallic heterostructures.[25–27,32] Impressively, this general idea for the templated growth of heterostructures can also be used for the preparation of metal–semiconductor[35] and semiconductor–semiconductor heterostructures.[36–38]

Acknowledgements

This work was supported by MOE under AcRF Tier 2 (ARC 26/13, No. MOE2013-T2-1-034; ARC 19/15, No. MOE2014-T2-2-093;

MOE2015-T2-2-057) and AcRF Tier 1 (RG5/13), and NTU under Start-Up Grant (M4081296.070.500000) in Singapore.

References

1 S. Linic, P. Christopher and D. B. Ingram, *Nat. Mater.*, 2011, **10**, 911–921.
2 Y. Xia, Y. Xiong, B. Lim and S. E. Skrabalak, *Angew. Chem., Int. Ed.*, 2009, **48**, 60–103.
3 Z. Fan, X. Huang, C. Tan and H. Zhang, *Chem. Sci.*, 2015, **6**, 95–111.
4 V. F. Puntes, P. Gorostiza, D. M. Aruguete, N. G. Bastus and A. P. Alivisatos, *Nat. Mater.*, 2004, **3**, 263–268.
5 N. Tian, Z.-Y. Zhou, S.-G. Sun, Y. Ding and Z. L. Wang, *Science*, 2007, **316**, 732–735.
6 X. Huang, Z. Zhao, L. Cao, Y. Chen, E. Zhu, Z. Lin, M. Li, A. Yan, A. Zettl, Y. M. Wang, X. Duan, T. Mueller and Y. Huang, *Science*, 2015, **348**, 1230–1234.
7 Z. Fan and H. Zhang, *Chem. Soc. Rev.*, 2016, **45**, 63–82.
8 Y. Sun, Y. Ren, Y. Liu, J. Wen, J. S. Okasinski and D. J. Miller, *Nat. Commun.*, 2012, **3**, 971.
9 Q. Li, L. Wu, G. Wu, D. Su, H. Lv, S. Zhang, W. Zhu, A. Casimir, H. Zhu, A. Mendoza-Garcia and S. Sun, *Nano Lett.*, 2015, **15**, 2468–2473.
10 K. Kusada, H. Kobayashi, T. Yamamoto, S. Matsumura, N. Sumi, K. Sato, K. Nagaoka, Y. Kubota and H. Kitagawa, *J. Am. Chem. Soc.*, 2013, **135**, 5493–5496.
11 M. Copel, M. C. Reuter, E. Kaxiras and R. M. Tromp, *Phys. Rev. Lett.*, 1989, **63**, 632–635.
12 C. P. Flynn, *Phys. Rev. Lett.*, 1986, **57**, 599–602.
13 Z. Q. Wang, S. H. Lu, Y. S. Li, F. Jona and P. M. Marcus, *Phys. Rev. B*, 1987, **35**, 9322–9325.
14 H. Li and B. P. Tonner, *Surf. Sci.*, 1990, **237**, 141–152.
15 H. Wormeester, E. Hüger and E. Bauer, *Phys. Rev. Lett.*, 1996, **77**, 1540–1543.
16 S. E. Habas, H. Lee, V. Radmilovic, G. A. Somorjai and P. Yang, *Nat. Mater.*, 2007, **6**, 692–697.
17 F.-R. Fan, D.-Y. Liu, Y.-F. Wu, S. Duan, Z.-X. Xie, Z.-Y. Jiang and Z.-Q. Tian, *J. Am. Chem. Soc.*, 2008, **130**, 6949–6951.
18 F. Wang, C. Li, L. D. Sun, H. Wu, T. Ming, J. Wang, J. C. Yu and C. H. Yan, *J. Am. Chem. Soc.*, 2011, **133**, 1106–1111.
19 B. Lim, M. Jiang, P. H. Camargo, E. C. Cho, J. Tao, X. Lu, Y. Zhu and Y. Xia, *Science*, 2009, **324**, 1302–1305.
20 M. R. Langille, J. Zhang, M. L. Personick, S. Li and C. A. Mirkin, *Science*, 2012, **337**, 954–957.
21 X. Xia, L. Figueroa-Cosme, J. Tao, H.-C. Peng, G. Niu, Y. Zhu and Y. Xia, *J. Am. Chem. Soc.*, 2014, **136**, 10878–10881.
22 B. T. Sneed, C.-H. Kuo, C. N. Brodsky and C.-K. Tsung, *J. Am. Chem. Soc.*, 2012, **134**, 18417–18426.
23 M. Grzelczak, B. Rodríguez-González, J. Pérez-Juste and L. M. Liz-Marzán, *Adv. Mater.*, 2007, **19**, 2262–2266.
24 X. Huang, S. Li, Y. Huang, S. Wu, X. Zhou, S. Li, C. L. Gan, F. Boey, C. A. Mirkin and H. Zhang, *Nat. Commun.*, 2011, **2**, 292.
25 Z. Fan, M. Bosman, X. Huang, D. Huang, Y. Yu, K. P. Ong, Y. A. Akimov, L. Wu, B. Li, J. Wu, Y. Huang, Q. Liu, C. E. Png, C. L. Gan, P. Yang and H. Zhang, *Nat. Commun.*, 2015, **6**, 7684.
26 Z. Fan, X. Huang, Y. Han, M. Bosman, Q. Wang, Y. Zhu, Q. Liu, B. Li, Z. Zeng, J. Wu, W. Shi, S. Li, C. L. Gan and H. Zhang, *Nat. Commun.*, 2015, **6**, 6571.
27 Z. Fan, Z. Luo, X. Huang, B. Li, Y. Chen, J. Wang, Y. Hu and H. Zhang, *J. Am. Chem. Soc.*, 2016, **138**, 1414–1419.
28 Z. Peng and H. Yang, *Nano Today*, 2009, **4**, 143–164.
29 R. Bauer, E. A. Jägle, W. Baumann and E. J. Mittemeijer, *Philos. Mag.*, 2011, **91**, 437–457.
30 S. Ithurria, P. Guyot-Sionnest, B. Mahler and B. Dubertret, *Phys. Rev. Lett.*, 2007, **99**, 265501.
31 S. C. Jain, A. H. Harker and R. A. Cowley, *Philos. Mag. A*, 1997, **75**, 1461–1515.
32 Z. Fan, Y. Zhu, X. Huang, Y. Han, Q. Wang, Q. Liu, Y. Huang, C. L. Gan and H. Zhang, *Angew. Chem., Int. Ed.*, 2015, **54**, 5672–5676.
33 H. L. Skriver, *Phys. Rev. B*, 1985, **31**, 1909–1923.
34 J. Gu, Y. Guo, Y.-Y. Jiang, W. Zhu, Y.-S. Xu, Z.-Q. Zhao, J.-X. Liu, W.-X. Li, C.-H. Jin, C.-H. Yan and Y.-W. Zhang, *J. Phys. Chem. C*, 2015, **119**, 17697–17706.
35 X. Huang, Z. Zeng, S. Bao, M. Wang, X. Qi, Z. Fan and H. Zhang, *Nat. Commun.*, 2013, **4**, 1444.
36 X.-J. Wu, J. Z. Chen, C. L. Tan, Y. H. Zhu, Y. Han and H. Zhang, *Nat. Chem.*, 2016, **8**, 470–475.
37 C. Tan, Z. Zeng, X. Huang, X. Rui, X.-J. Wu, B. Li, Z. Luo, J. Chen, B. Chen, Q. Yan and H. Zhang, *Angew. Chem., Int. Ed.*, 2015, **54**, 1841–1845.
38 C. Tan and H. Zhang, *J. Am. Chem. Soc.*, 2015, **137**, 12162–12174.